RESEARCH ARTICLE

Olivine diffusion constrains months-scale magma transport within Kīlauea volcano's summit reservoir system prior to the 2020 eruption

Kendra J. Lynn[1] · Patricia A. Nadeau[1] · Dawn C. S. Ruth[2] · Jefferson C. Chang[1] · Peter J. Dotray[1] · Ingrid A. Johanson[1]

Abstract

The unprecedented 2018 summit collapse at Kīlauea and subsequent 2020–2021 eruption within the newly deepened Halemaʻumaʻu Crater provide an unparalleled opportunity to understand how collapse events impact a volcano's shallow reservoir system and magmatic processes. Glass and olivine from tephra ejected by lava fountains and several explosions on 20–21 December, within a few hours of the 2020 eruption onset, yield information about pre-eruptive magma storage and transport. The olivine population is bimodal with zoned and non-zoned phenocrysts. Normally zoned olivine crystals with core compositions around Fo_{88} have 30–50 μm wide Fo_{82} overgrowth rims that have skeletal textures. Two skeletal xenocrysts (cores Fo_{74} and Fo_{81}) are also reversely zoned up to Fo_{82} rims. The crystal cores have trace element records of at least two cycles of growth and dissolution prior to the formation of the overgrowth rims. These rims and a separate population of non-zoned Fo_{82} crystals are in Fe–Mg equilibrium with their host glass (average MgO of 6.9 ± 0.4 wt% (1σ), Mg# [Mg / (Mg + Fe^{2+})] of 0.57), which suggests undercooling after intrusion of magma to shallow levels in the plumbing system. In the years prior to the 2018 collapse, non-zoned Fo_{81} olivine and slightly lower MgO glasses (6.8 wt%) reflected continuous mixing and compositional buffering of magma recharge into several km^3 of stored magma in the Halemaʻumaʻu reservoir (1–2 km depth). The 2020 olivine crystals lack evidence of an intrusion mixing with resident shallow magma, indicating that magma transport occurred in a disrupted system, and/or it may not have significantly mixed with stored magma remaining in the Halemaʻumaʻu reservoir after the events of 2018. Diffusion modeling of Fe–Mg exchange in the zoned 2020 olivine crystals yield timescales that are mostly 60 days prior to the eruption or less, which aligns well with 22–24 October 2020 and subsequent seismic swarms at Nāmakani Paio ∼ 5 km west of Kīlauea's summit caldera. This correlation indicates that magma intruding beneath the summit (volume accommodation, recorded by the olivine crystals) was expressed by tectonic earthquakes along the Kaʻōiki fault zone (stress accommodation). The absence of precursory SO$_2$ within minutes prior to eruption also indicates that the 2020 December magma may have risen from 1 to 2 km depth to the surface in as little as 10 min.

Keywords Kīlauea · Hawaiʻi · Halemaʻumaʻu · Olivine diffusion

Introduction

Monitoring seismicity, ground deformation, and gas release of volcanic systems in real time provides rich datasets that yield insights into changes in volcano behavior. An ongoing challenge, however, is interpreting which subsurface magmatic processes these signals reflect, including magma recharge, mixing, and pre-eruptive degassing. Multi-disciplinary studies often provide the best links between monitoring data and processes. Diffusion chronometry, which constrains the timescales of magmatic processes, is now a widely used petrologic tool that enhances our ability to

✉ Kendra J. Lynn
  klynn@usgs.gov

1   US Geological Survey, Hawaiian Volcano Observatory, 1266 Kamehameha Avenue Suite A8, Hilo, HI 96721, USA

2   US Geological Survey, California Volcano Observatory, Moffett Field, CA 94035, USA

understand records of pre-eruptive magma storage, transport, ascent, and eruption (e.g., Dohmen et al. 2017; Costa et al. 2020 and references therein). Linking these petrological timescales with geodetic, seismic, and/or gas monitoring records provides an important framework for understanding both contemporary and much older eruptions at volcanic systems around the globe (e.g., Kahl et al. 2011; Saunders et al. 2012; Kilgour et al. 2014; Hartley et al. 2016; Rasmussen et al. 2018).

Kīlauea (Island of Hawaiʻi) is one of the most intensely monitored and best-studied volcanoes in the world (e.g., Tilling and Dvorak 1993; Anderson et al. 2019, 2024; Neal et al. 2019) and is ideally suited for interdisciplinary studies that leverage diffusion chronometry. Its summit magma storage system is thought to be comprised of two primary magma reservoirs underneath the summit: one at 1–2 km depth referred to as the Halemaʻumaʻu reservoir and a deeper reservoir to the south of the summit caldera referred to as the south caldera reservoir (e.g., Poland et al. 2014). In the past 200 years, summit eruptions have been sourced from either reservoir (e.g., Pietruszka and Garcia 1999; Garcia et al. 2003; Pietruszka et al. 2015; Lerner et al. 2021; Wieser et al. 2021), as well as deeper sources that at least partially bypassed this system (e.g., 1959 Kīlauea Iki; Helz 2022; see also Anderson et al. 2024 for recent summary of debated summit reservoir geometries and connections).

Kīlauea's recent eruptions between 1983 and 2023 both at the summit and on the East Rift Zone have provided unparalleled opportunities to characterize how magmas transit the volcano's reservoir system (e.g., Neal et al. 2019; Poland et al. 2014 and references therein). Kīlauea's unprecedented East Rift Zone eruption in 2018 induced coeval summit collapse and partially drained the shallow Halemaʻumaʻu magma reservoir (11–33% evacuation of magma at 1–2 km depth; Anderson et al. 2019) and also probably disrupted and/or destroyed shallow magma pathways connecting reservoirs to the surface (Lynn and Swanson 2022). The years following the 2018 events included the formation of Kīlauea's first summit water lake in written history (Nadeau et al. 2020; Flinders et al. 2021), a significant increase in deep Pāhala seismicity (Burgess and Roman 2021; Wilding et al. 2022), reinflation of the summit and East Rift Zone storage systems (Poland et al. 2019; Wang et al. 2021; Segall et al. 2022; Anderson et al. 2024), high rates of south flank motion (Anderson et al. 2024), and finally renewed eruptive activity at Kīlauea starting in December 2020. Given these considerable changes and the appearance of a water lake inside the Halemaʻumaʻu collapse crater (Nadeau et al. 2020; Flinders et al. 2021), interpreting monitoring data and corresponding magmatic processes leading up to the 2020–2021 summit eruption was challenging.

Here, we leverage olivine chemistry from the tephra collected from the first ~21 h of the 2020–2021 eruption at Halemaʻumaʻu to provide the first geochemical insights on the state of Kīlauea's shallow reservoir system following the 2018 summit collapse. Constraining magma storage and transport via olivine diffusion chronometry is a robust approach at Kīlauea because olivine is the only phenocryst phase to crystallize for > 100 °C below the liquidus (Wright and Okamura 1977; Wright and Peck 1978), and experimentally determined diffusion coefficients for Fe–Mg exchange in olivine are well characterized at basaltic temperatures (e.g., Chakraborty 2010 and references therein). The December 2020 olivine diffusion timescales correlate remarkably well with 4 months of pre-eruptive seismicity and deformation signals at Kīlauea's summit. Most timescales coincide with earthquake swarms that began west of the summit about 2 months prior to eruption. Virtually none of the timescales correlate with a significant summit intrusion event 18 days prior to eruption, indicating that this intrusion was not the source of the eruption. Pre- and syn-eruptive gas monitoring data, combined with seismic data, also suggest that the 2020–2021 eruption magmas may have ascended from 1 to 2 km depth to the surface in 10 min or less prior to eruption onset.

Eruption and sample overview

Two months after the end of the 2018 eruption saw the return of deflation-inflation (DI) events at the summit of Kīlauea, suggesting that the shallow Halemaʻumaʻu reservoir was receiving magma recharge (Poland et al. 2019). By March 2019, the summit began to steadily inflate with a major increase in rates of uplift beginning in September 2020. Seismicity became elevated starting in October 2020, with multiple earthquake swarms occurring under Kīlauea's summit, upper East Rift Zone, and the Kaʻōiki fault zone west of the summit. From 30 November–2 December, a significant swarm under the summit and several pulses of heightened activity in the East Rift Zone precluded the first post-2018 dike intrusion under the southern part of the summit caldera (Ellis et al. 2023). Following this intrusion, long-period seismic signals were observed with increasing frequency.

On the night of 20 December 2020, an earthquake swarm in the upper East Rift Zone around 19:30 HST preceded a significant increase in summit earthquakes, the rate of which rapidly intensified until 21:20 HST. Spasmodic tremor then dominated the signals for ~10 min, after which the eruption began at approximately 21:29 HST in Halemaʻumaʻu (Fig. 1a). Three fissures opened in the north and west crater walls (Fig. 1b), effusing lava down into and rapidly boiling off the summit water lake (Cahalan et al. 2023). Most of the eruption occurred via the north and west fissures, which were characterized by sustained vigorous lava fountains (Fig. 1a, b), of which the north fountain was active

Fig. 1 Eruption and sample characteristics. **a** Map of Kīlauea's summit region on the Island of Hawai'i (inset map) showing the location of the north and west fissures (red circles) in Halema'uma'u. Symbols denote positions of the location of studied tephra sample (white star) as well as permanent global positioning system (OUTL, AHUP, CRIM, UWEV; blue squares), tiltmeter (UWE; green diamond), and gas monitoring (MG21_KIL, HRSDH; yellow hexagons) stations. Region of Nāmakani Paio earthquakes denoted by blue transparent circle. Basemap generated from Mosbrucker et al. (2020), a 2005 NOAA digital terrain model (Office for Coastal Management 2015), and a 1983 USGS digital elevation model (US Geological Survey 1983). **b** The Halema'uma'u eruption on the evening of 20 December 2020 began at approximately 21:30 HST with fissures opening in the west and north walls of Halema'uma'u. This photo is viewing down into the crater from the west, looking toward the east. **c** View to the southwest of Crater Rim Drive (accessed with permission from, and in coordination with, Hawai'i Volcanoes National Park) on the afternoon of 21 December. The road was covered by a layer of tephra from the opening of the fissures. A dense gas plume from the eruption obscures the intensity of the sun. The sample in this study was taken from an undisturbed area of the road surface. **d** The 2020 tephra is composed of both glassy and dull juvenile material from which olivine crystals were picked. USGS Photos
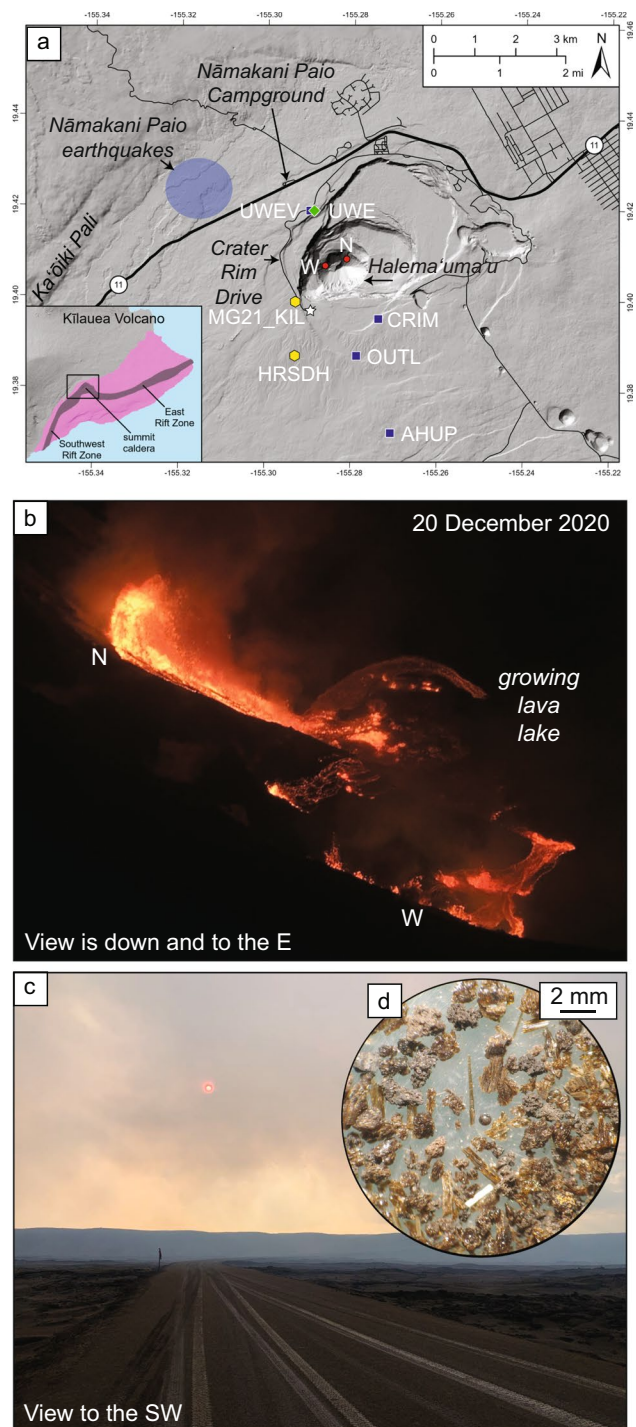

for 6 days before the rising lava lake drowned the vent. The eruption continued for 5 months with effusion of lava into Halema'uma'u, ending in May 2021.

The lava fountains generated a plume of tephra and gas that drifted to the southwest as a result of the prevailing trade winds. Glass and olivine in this study were analyzed from air-quenched tephra ejected by the eruptive vents on 20–21 December. Sample KS20-527 was collected at 18:15 HST on 21 December 2020 on Crater Rim Drive (19.39863, -155.291966; Fig. 1c) from an undisturbed surface of the road within a closed area of Hawai'i Volcanoes National Park. This sample represents all accumulated tephra at this location over the first ~ 21 h of the 2020–2021 eruption and is primarily composed of glassy and dull juvenile lapilli with Pele's hairs and tears (Fig. 1d). No additional significant deposits of tephra were generated for the rest of the 2020–2021 eruption, which remained completely within Halema'uma'u, and thus was inaccessible for sampling. The 20–21 December tephra sample was sieved into 0.5–1.0 mm and 1–2 mm size fractions, which were picked for olivine crystals that were subsequently mounted in a 2.5 cm diameter epoxy puck and ground to expose crystal cores.

Methods

Scanning electron microscope (SEM)

Olivine crystals were first categorized based on zoning patterns evident in backscattered electron (BSE) images obtained using a Hitachi S-3400N SEM at the University of Hawai'i at Hilo. Compositional surveys were also conducted using the university's Oxford 80 mm energy dispersive spectroscopy (EDS) detector using a working distance of 10 mm and beam conditions of 20 kV and 50–60 nA current. Olivine crystal orientations, necessary for addressing diffusion anisotropy, were determined using a TESCAN Vega3 SEM with Oxford Symmetry electron backscatter detector (EBSD) at the US Geological Survey lab in Menlo Park, California. Measurements were taken using a 70° sample tilt, 15–20 kV accelerating voltage, and working distance

between 17.5 and 20 mm. Area maps of whole or half olivine crystals achieved mean angular deviation values of < 1°. Orientations were plotted in lower equal-area (Schmidt) hemisphere stereonet projections and α, β, and γ, the angles between the traverse and the *a*-, *b*-, and *c*-axes of the olivine crystal, respectively, were calculated using the *Stereonet* software (Cardozo and Allmendinger 2013).

Electron probe microanalyses (EPMA)

Olivine core-to-rim traverses were measured using a five spectrometer JEOL Hyperprobe JXA-8500F at the University of Hawai'i at Mānoa using a 15 kV accelerating voltage and a 1 μm beam with a 50 nA current. Major elements Si, Mg, and Fe were gathered using combined EDS analyses on a Thermo UltraDry detector using a SystemSix analyzer with a dead time of 38% and live acquisition for 60 s. Ca, Ni, and Mn were measured by wavelength dispersive (WDS) spectrometers, and counting times were 60 s with 20 s on both sides of the peak for backgrounds. Al and P were also measured by WDS spectrometer but were almost always below detection (0.02 wt% for P and 0.01 wt% for Al) and are not discussed further. San Carlos olivine (USNM 111312/444; Jarosewich et al. 1980) was measured regularly throughout the analyses to monitor for instrumental drift. Standards were Springwater olivine (USNM 2566) for Si, Fe, and Mg, a synthetic nickel-oxide for Ni, Verma garnet for Mn, and Kakanui Augite (USNM 122142; Jarosewich et al. 1980) for Ca. Two-sigma relative precision, based on repeated analyses of San Carlos olivine, are 0.24 wt% for SiO_2 and MgO, 0.20 wt% for FeO, 0.02 wt% for MnO and NiO, and 0.01 wt% for CaO (Supplementary Data). X-ray intensities were converted to concentrations using standard ZAF corrections (based on atomic number (Z), absorption (A), and fluorescence excitation (F); Armstrong 1988). Analyses with totals < 99.0 or > 100.5 wt% were rejected. Olivine core and adhering glass compositions were previously published to characterize the populations in the 2020 Halema'uma'u eruption (Lynn 2022) and were measured in the same laboratory.

X-ray element maps of P (two spectrometers; PETL), Al (TAPL), Cr (LIFL), and Ca (PETJ) were collected using WDS on the JEOL Hyperprobe JXA-8530F at the US Geological Survey lab in Menlo Park for two olivine crystals from the diffusion modeling suite. Analytical conditions were 15 keV, 200 nA, resolutions of 1 μm/pixel, and dwell times of 300 ms/pixel.

Diffusion modeling

Compositional gradients in Fo were modeled using finite differences and the one-dimensional form of Fick's Second Law (Crank 1975):

$$\frac{\partial C}{\partial t} = D \frac{\partial^2 C}{\partial x^2} \tag{1}$$

where C is concentration, t is time (in seconds), D is the diffusion coefficient (in m^2/s), and x is distance (in m). The concentration-dependent diffusion coefficient for Fe–Mg exchange in olivine was calculated using:

$$D_{Fe-Mg} = 10^{-9.21} \left(\frac{f_{O_2}}{10^{-7}} \right)^{\frac{1}{6}} 10^{3(X_{Fe}-0.1)} \exp \left(-\frac{201000 + (P-10^5)(7 \times 10^{-6})}{RT} \right) \tag{2}$$

where f_{O_2} is the oxygen fugacity (in Pa), X_{Fe} is the mol fraction of iron in the olivine, P is the pressure (in Pa), R is the ideal gas constant, and T is the temperature (in Kelvin; Dohmen and Chakraborty 2007a, b). This expression is for diffusion along the *c*-axis, which is six times faster than diffusion along the *a*- or *b*-axes. To account for diffusion anisotropy, a modified diffusivity was calculated using the measured orientations of the principal crystallographic axes relative to the traverse direction (Costa and Chakraborty 2004):

$$D_{trav}^{Fe-Mg} = D_a^{Fe-Mg}(\cos\alpha)^2 + D_b^{Fe-Mg}(\cos\beta)^2 + D_c^{Fe-Mg}(\cos\gamma)^2 \tag{3}$$

where α, β, and γ are the angles between the traverse and the *a*-, *b*-, and *c*-axes of the olivine crystal, respectively. These were calculated from EBSD-determined orientations plotted in *Stereonet* (Cardozo and Allmendinger 2013).

The initial condition (C_i) was determined based on the Fo content (forsterite; [Mg / (Mg + Fe^{2+}) × 100]) of the plateau through the olivine core. The boundary condition (C_o) was set to the Fo content of the olivine rim. Zoned crystals in this study required a step function to represent the overgrowth rim, and the width of this rim was determined by using the location of sharp increases in CaO content that reflect crystal growth.

Intrinsic environmental parameters required for the models are relatively well constrained for Kīlauea. The likely temperature at which diffusive re-equilibration occurred was determined using a suite of olivine-melt experimental data (Helz and Thornber 1987; Montierth et al. 1995; Matzen et al. 2011; Shea et al. 2022) and a new thermometer calibrated for this dataset (Shea et al. 2022) to assess an Fe–Mg equilibrium temperature for a given Fo content. Because the olivine overgrowth rims consistently recorded Fo_{82} compositions, a temperature of 1200 °C was used for all the diffusion models (similar to Mourey et al. 2023). This is akin to the magma temperature for pre-eruptive storage and diffusion recorded by all the olivine crystals. Oxygen fugacity was set relative to the quartz-fayalite-magnetite buffer at QFM + 0.4 based on $Fe^{3+}/\sum Fe$ measurements in Kīlauea Iki melt inclusions, representing likely pre-eruptive redox conditions (Helz et al. 2017). The pressure was set to 45 MPa

reflecting the approximate pressure at the center of the pre-collapse Halemaʻumaʻu reservoir at 1–2 km (Poland et al. 2014; Anderson et al. 2019).

Timescales were determined by reducing the misfit between the measured data and the diffusion model through root mean square deviation calculations in MATLAB, which finds the best fit to the microprobe data:

$$RMSD = \sqrt{\frac{\sum_M \left(C_{real}^i - C_{model}^i\right)^2}{M}} \tag{4}$$

where M is the number of points along the profile, i is the coordinate along the profile, C_{real} is the measured concentration, and C_{model} is the concentration in the diffusion model that is being evaluated (cf., Shea et al. 2015a). Microprobe data were considered with a 2σ precision of 0.2 mol% Fo based on repeated measurements of the San Carlos Olivine standard (Supplementary Data).

Results

The 2020 tephra olivine population is bimodal (Lynn and Swanson 2022), with populations of non-zoned and normally zoned phenocrysts (> 0.5 mm diameter). Non-zoned phenocrysts predominantly have Fo_{82} compositions, with two rare non-zoned crystals at higher Fo (87 and 89; Fig. 2a). The non-zoned olivine crystals almost always have skeletal textures (Fig. 2b). The other major population comprises normally zoned olivine crystals ($Fo_{core} > Fo_{rim}$; Fig. 2c) that have Fo_{86-89} cores but is dominated by Fo_{88} compositions (Fig. 2a). Normally zoned crystals have rim compositions that are Fo_{81-84}. Two of the zoned olivine have lower Fo cores (72 and 80; Fig. 2d) and are reversely zoned, where $Fo_{core} < Fo_{rim}$ (Fig. 2d). Additionally, one crystal has subtle complex zoning, herein referred to as the "shoulder" type because the crystal has slight reverse zoning from the core, which changes to normal zoning in the outer portion of the crystal rim (Fig. 2e). Almost all zoned crystal rims and all non-zoned olivine crystals are in Fe–Mg equilibrium with their host glasses (Fig. 2f), which have an average MgO of 6.9 ± 0.4 wt% (1σ; Lynn 2022) and Mg# [Mg / (Mg + Fe²⁺)] of 0.57 (calculated assuming $Fe^{3+}/\sum Fe = 0.17$, Helz et al. 2017 and the equilibrium field of Roeder and Emslie 1970). Zoned olivine cores typically plot above the equilibrium field, indicating that they are out of equilibrium with the melts that carried them to the surface.

All zoned olivine crystals have 30–50 μm wide overgrowth rims that exhibit different degrees of skeletal to polyhedral textures (Fig. 2) and are mostly Fo_{82} in composition (Fig. 3a). The overgrowth rims are also clearly defined by abrupt changes in CaO content within 30–50 μm of crystal rims (Fig. 3b), which are inferred to reflect relatively recent crystal growth due to the much slower diffusivity of Ca compared to Fe–Mg (e.g., Coogan et al. 2005). Zoning patterns for NiO mimic those shown by Fo (Fig. 3c), but NiO zoning is generally less developed (i.e., decoupled from Fo, where the width of zoning for Ni is smaller than for Fo; e.g., Lynn et al. 2017b; Schleicher 2017). NiO profiles are not modeled for diffusion timescales in this study for several reasons. First, the experimentally determined diffusion coefficient for Ni is overall less well characterized than for Fe–Mg exchange (e.g., Petry et al. 2004; Holzapfel et al. 2007; Chakraborty 2010 and references therein). Because the Arrhenius relationships for Fe–Mg and Ni are not parallel, the discrepancies between Fo and Ni-derived timescales vary with temperature (Costa and Dungan 2005; Lynn et al. 2017a). Second, previous diffusion studies of Kīlauea olivine showed that most of the Ni timescales were shorter than those derived from Fo and did not agree within error (Lynn et al. 2017a). Similar discrepancies in other volcanic systems (e.g., Tatara-San Pedro, Costa and Dungan 2005; Shiveluch, Gordeychik et al. 2018; Paricutin, Albert et al. 2020; Klyuchevskoy, Gordeychik et al. 2020) were inferred to be the result of the less well characterized Ni diffusion coefficient (Gordeychik et al. 2020).

The Fo_{88-89} crystals have NiO contents 0.39–0.42 wt%, similar to other Kīlauea olivine compositions (e.g., Lynn et al. 2017b) and primarily follow a fractional crystallization trend (Fig. 4a; Wang and Gaetani 2008). The Fo_{82} rims and non-zoned crystals have NiO contents of 0.22–0.23 wt%, which is also consistent with fractional crystallization trends and supports inferences that rims were formed by recent overgrowths. CaO contents are low (0.21–0.24 wt%) for the high-Fo crystal cores (Fig. 4b). The Fo_{82} rims have higher CaO, ranging from 0.27 to 0.31 wt%, and are largely distinct from the Fo_{82} non-zoned crystals, which are slightly lower with 0.26–0.28 wt% CaO.

X-ray element maps of two olivine crystals (Ol. 11 and Ol. 13) from the diffusion dataset show clear changes in Ca (also shown in Fig. 3b) and P concentration between high-forsterite cores and low-forsterite rims (Fig. 5). The widths of the low-forsterite rims are greater than the widths of the Ca and P overgrowth rims, indicating that the low-forsterite rims have undergone some degree of diffusive re-equilibration with the neighboring high-forsterite cores. Phosphorus maps also show older resorbed cores within the high-forsterite zones, as evidenced by the sharp, curved truncations of P zoning that reflect dissolution fronts (e.g., Mourey et al. 2023).

Twenty diffusion timescales calculated from Fe–Mg zoning in 19 olivine crystals (two times obtained for the complexly zoned crystal) vary from 14–521 days (Table 1; see also Supplementary Data for full analytical profiles and diffusion model inputs and outputs). There are no systematic differences in modeled timescales among the normal, reverse, or complexly
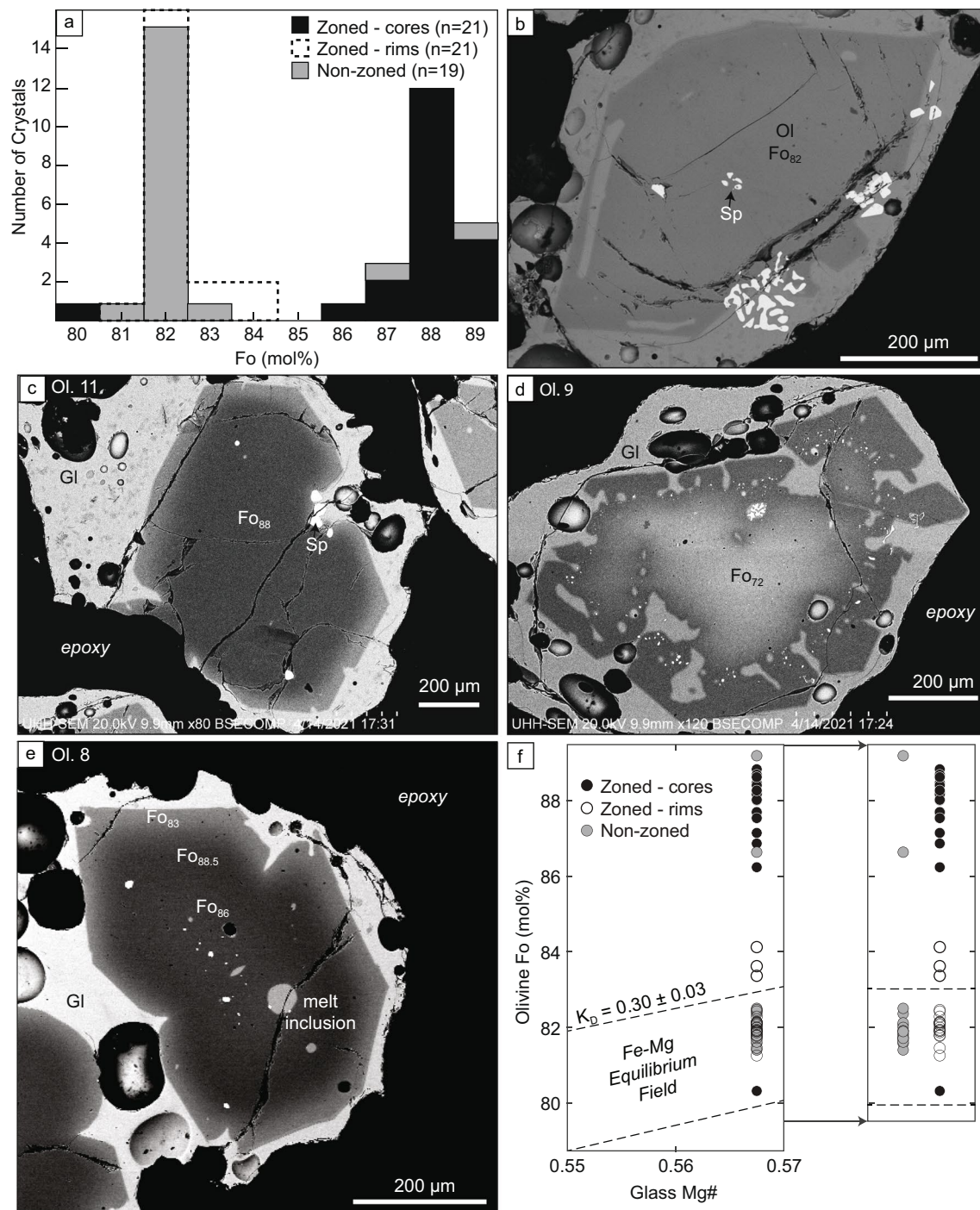
Fig. 2 Overview of olivine compositions and textures. **a** Histogram of olivine compositions for the non-zoned (gray) and zoned (black) populations. Bins represent 1 mol% (e.g., $Fo_{87.5}$ to $Fo_{88.4}$). One zoned core (not shown) has a composition of Fo_{72}. Rim compositions for zoned olivine crystals are shown by dashed black line. **b** Backscattered electron (BSE) image of representative non-zoned olivine crystal. **c** BSE image of normally zoned olivine crystal, where $Fo_{core} > Fo_{rim}$. **d** BSE image of rare reverse zoned olivine crystal, where $Fo_{core} < Fo_{rim}$. **e** BSE image of rare complexly zoned olivine crystal, with reversely zoned interior and normally zoned outer rim. **f** Glass Mg# [Mg# = Mg/(Mg + Fe^{2+})] plotted against zoned cores (black circles; data from Lynn 2022) and rims (open circles) and non-zoned cores (gray circles). The panel on the right shows the same data but with the populations separated for clarity. The dashed lines show the shallow pressure (1 atm) Fe–Mg equilibrium field ($K_D^{Fe-Mg} = 0.30 \pm 0.03$) of Roeder and Emslie (1970). Mg# is calculated assuming Fe^{3+}/ΣFe = 0.17 based on recent μ-XANES analyses of undegassed Kīlauea olivine-hosted melt inclusions (Helz et al. 2017). Zoned olivine cores typically plot above the equilibrium field and represent non-equilibrium conditions whereas zoned rims and non-zoned cores lie within the field, suggesting that they are in Fe–Mg equilibrium with the melts that carried the olivine crystals to the surface
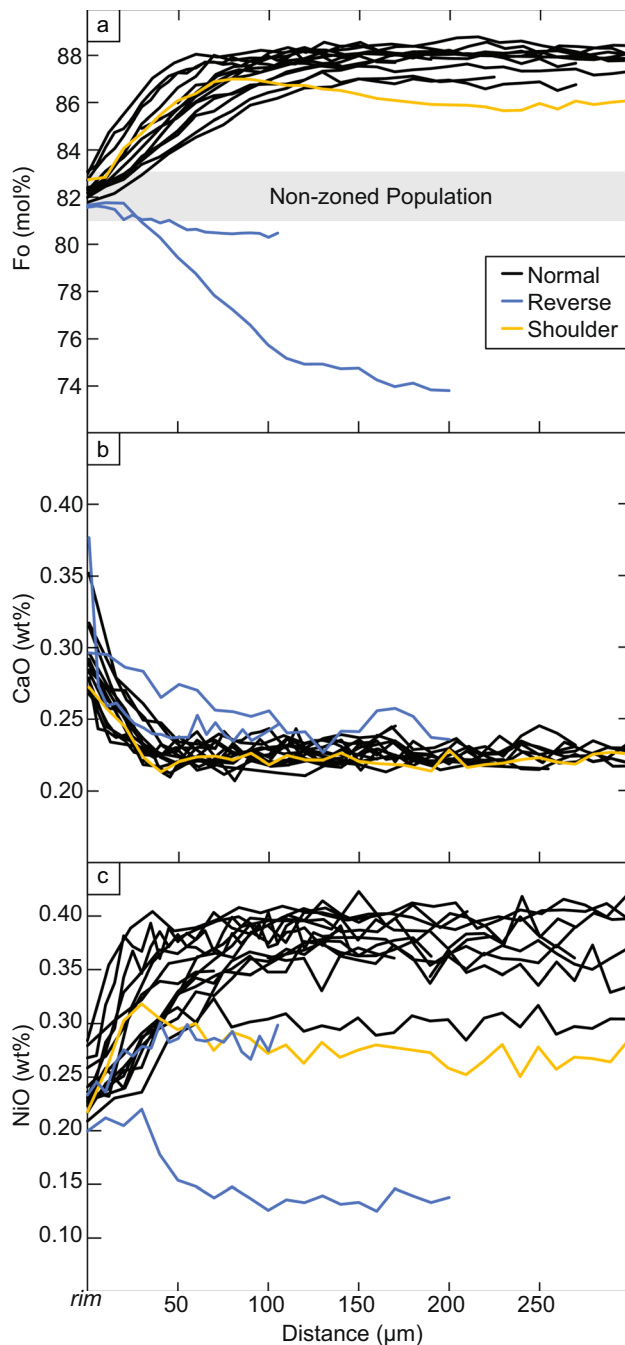
Fig. 3 Olivine profiles used for diffusion models. **a** Forsterite profiles show that the zoned population is dominated by normal zoning (black lines) with a few reversely zoned crystals (blue lines). One olivine crystal showed subtle complex zoning, with a reversely zoned core and a normally zoned rim ("shoulder" type, yellow line). All profiles zone toward Fo_{82-83} rims, the same composition as the non-zoned olivine population. **b** CaO profiles all have 30–50 μm wide rims that increase in CaO, marking crystal growth. The width of the CaO zoning is used to set the boundary conditions for each diffusion model. **c** NiO profiles generally mimic the zoning patterns shown by Fo but are decoupled because their zoning widths are narrower
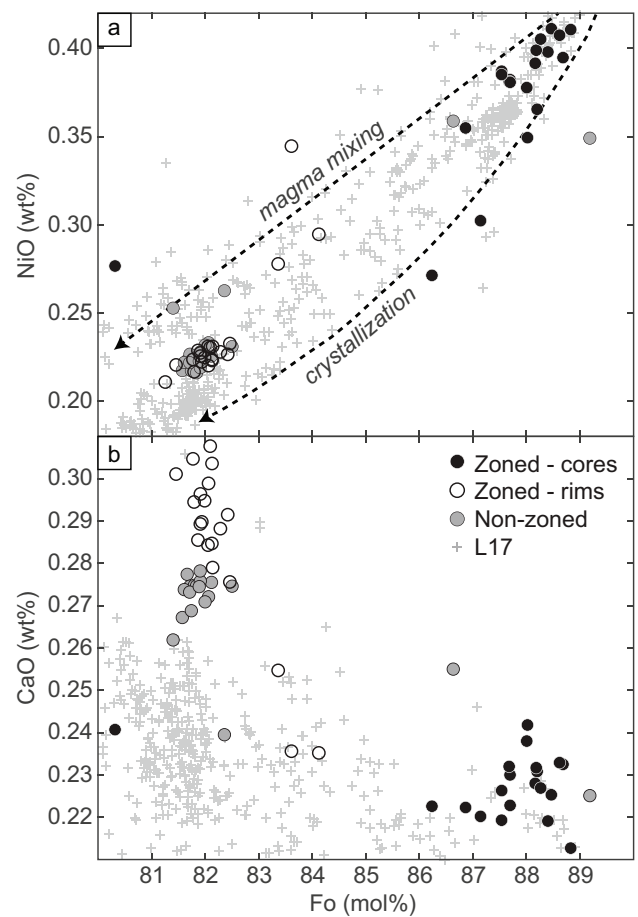

Fig. 4 Minor element variations in 2020 olivine compared to other Kīlauea olivine core compositions (gray + symbols; Lynn et al. 2017b). **a** NiO contents indicate olivine composition is dominantly controlled by fractional crystallization. Evidence for magma mixing is minimal. **b** Zoned olivine rims have higher CaO compared to non-zoned olivine cores, which results from rapid overgrowth of rims on high-Fo cores

zoned crystals. Most crystals (68%) yield calculated timescales of 4 months or less and over half (53%) record 3 months or less (Fig. 6). Errors are mostly related to the temperature uncertainty (± 10 °C; Helz and Thornber 1987) and are typically $\pm 30\%$ relative to the timescale calculated for each olivine profile (e.g., a 10-day timescale has a ± 3-day uncertainty; Lynn et al. 2017b; Lynn and Helz 2023).

Discussion

Olivine populations and their zoning patterns yield critical insights into the magma storage and transport history leading to Kīlauea's 2020–2021 eruption. These data also
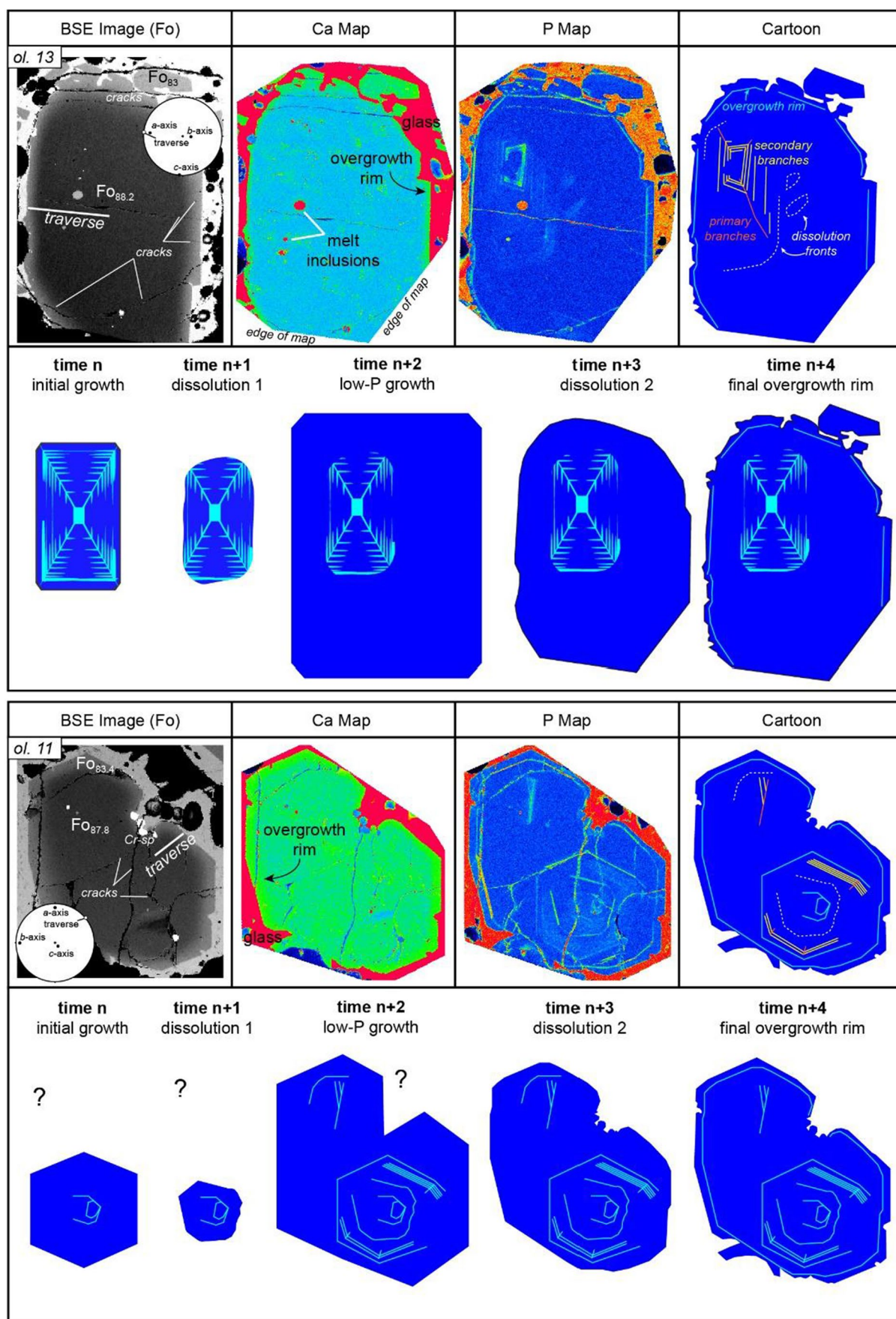
◀**Fig. 5** Backscattered electron (BSE) images and qualitative X-ray maps of Ca and P in normally zoned olivine from the 2020 eruption. The sharp truncations in P zoning (illustrated by dashed lines in cartoons) record dissolution events that separate early high-Fo cores from later high-Fo overgrowths, and finally the latest low-Fo overgrowth rims. Primary (orange lines) and secondary (yellow lines) branches represent the dendritic framework of the crystals (after Mourey et al. 2023). Dashed white lines are dissolution features within the olivine cores. Question marks in bottom panel indicate that the earliest growth history of the left side of this crystal is unclear

provide clues about how the summit reservoir system and its dominant magmatic processes have changed following the significant summit collapse in 2018—a type of event expected to strongly affect the shallow emplacement and transfer of magma in active volcanoes (Corbi et al. 2015) and the magmatic processes affecting the evolution of ascending magmas (Gavrilenko et al. 2016). Below, we identify key differences between the pre- and post-collapse magmatic processes in Kīlauea's shallow reservoir system and outline the magma emplacement, storage, and ascent history for the December 2020 eruption.

Different magmatic processes pre- versus post-collapse

Despite the limited time series of olivine chemistry for the 2020–2021 eruption, the 20 December tephra clearly shows that the summit collapse in 2018 led to some notable changes in both Kīlauea's shallow plumbing system and its magmatic processes. Prior to the 2018 summit collapse, non-zoned Fo_{81} olivine and lower MgO glasses (e.g., 6.8 wt%; Gansecki et al. 2019; Lynn 2022) from the summit lava lake reflected continuous mixing, compositional buffering, and fractional crystallization of magma recharge in the well-established Halemaʻumaʻu reservoir at 1–2 km depth (Thornber et al. 2015; Lynn and Swanson 2022). The Fo_{88} normally zoned olivine crystals in the 20 December tephra strongly contrast with the pre-2018 non-zoned Fo_{81} lava lake olivine crystals. The presence of Fo_{88} olivine crystals in the 20 December tephra is significant because this is the first instance of high-Fo olivine erupted from Kīlauea's summit since the opening weeks of the 2008–2018 Halemaʻumaʻu lava lake (Mourey et al. 2022, 2023).

During the 2018 lower East Rift Zone eruption, the shallow Halemaʻumaʻu reservoir was only partially drained (11–33% of the volume removed; Anderson et al. 2019), yet the 2020 olivine cargo lacks strong evidence of mixing with stored magma containing a resident population of lower Fo olivine crystals. For example, there is not a significant population of low-Fo olivine that is reversely zoned toward a similar rim composition as the high-Fo normally zoned crystals (cf. Lynn et al. 2017a). This absence suggests that the 20 December eruption magma may not have

significantly mixed with stored magma leftover from prior to the 2018 summit collapse, or magma that began accumulating as early as 2 months after the end of the 2018 eruption (Poland et al. 2019). This may indicate that the 2020 magma was new and unrelated to magmas intruding following the 2018 eruption. The longest diffusion timescale was 521 days, or ~ 17 months prior to eruption (Table 1) and would correspond to July 2019 and could possibly be related to the earlier refilling of the summit reservoir system (Poland et al. 2019). The 2020 eruptive activity waned quickly after 20–21 December and no other substantial tephra deposits formed beyond the collapse crater for the duration of the 2020–2021 eruption, so there are no olivine crystals to confirm whether remnant 2018 summit magma might have subsequently erupted. Additional geochemical studies of this and other recent Kīlauea eruptions (2021–2022, January 2023, June 2023, and September 2023) will be critical for evaluating this question.

Undercooling prompted olivine rim growth and subsequent diffusion

The skeletal textures and uniform compositions of the rims on the zoned crystals as well as the non-zoned population indicate recent and rapid crystal growth (e.g., Faure and Schiano 2004; Faure et al. 2007). Further evidence for rapid growth is found in the abrupt increases of CaO on zoned crystal rims (Fig. 3), which are caused by a localized increase in the Ca partition coefficient due to the buildup of Ca in melt boundary layers during growth (Lang et al. 2021). Overgrowth rims are also evident in X-ray element maps of select 2020 olivine crystals (Fig. 5), wherein Ca and P zoning are correlated in crystal rims, marking a late stage of rapid growth (e.g., Milman-Barris et al. 2008; Welsch et al. 2013, 2014; Shea et al. 2019; Mourey et al. 2023). Phosphorus zoning links major (Fe–Mg) and minor (Ca) element zoning patterns to crystal growth and dissolution cycles because P diffusion is much slower than Fe–Mg (Shea et al. 2019) and thus preserves a longer-term magmatic history (e.g., de Maisonneuve et al. 2016).

We propose that the overgrowth rims are the result of high degrees of undercooling (Jambon et al. 1992) after magma carrying high-Fo olivine intruded to shallow levels in the plumbing system. The Fo_{82} compositions of the skeletal rims and the non-zoned crystals suggest depths of 1–2 km in the Halemaʻumaʻu reservoir (Cervelli and Miklius 2003; Poland et al. 2014) that produced Fo_{81} olivine crystals after the 2008–2018 lava lake (which presumably drew from the top of that reservoir; e.g., Gansecki et al. 2019; Lynn 2022) was established. The likely source of the intruding magma in 2020 is from the south caldera reservoir (3–5 km depth; Cervelli and Miklius 2003; Poland et al. 2014), from which Fo_{88} olivine in the 2018 lower East Rift Zone eruption

Table 1 Calculated timescales and modeling parameters for the diffusion of Fe–Mg in olivine crystals

Olivine ID	Zoning type	C_i	C_o	t (days)	$\pm$ (days)
1	Normal	88.5	82.4	187	56
2	Normal	88.5	82.0	30	9
3	Normal	87.5	82.0	64	19
5	Normal	87.9	82.4	238	71
7	Normal	88.0	82.3	43	13
10	Normal	88.2	82.0	326	98
11	Normal	87.8	83.4	39	12
12	Normal	88.0	82.7	51	15
13	Normal	88.2	83.0	60	18
15	Normal	88.0	83.1	521	156
16	Normal	87.0	82.0	54	16
18	Normal	88.1	83.0	112	34
20	Normal	88.8	82.8	463	139
21	Normal	88.8	83.0	85	26
22	Normal	88.7	84.4	44	13
23	Normal	88.6	83.6	259	78
9	Reverse	73.8	81.7	97	29
19	Reverse	80.5	81.7	14	4
8	Shoulder	85.8	88.5	137	41
	t_1 out		82.8	41	12

C_i is the initial condition set by the core composition and C_o is the boundary condition set by the rim composition, both reported as Fo (forsterite; [Mg / (Mg + Fe) × 100])

were thought to be sourced (e.g., Lerner et al. 2021; Wieser et al. 2021). Melt inclusions in high-Fo 2018 olivine crystals yield calculated entrapment temperatures of 1250–1310 °C (Lerner et al. 2021), which could reflect the temperature of magma intruding upward from the south caldera reservoir. It would have subsequently been in Fe–Mg equilibrium with a 1200 °C magma (see temperature calculation in the "Methods" section above) at the depth of the Halemaʻumaʻu reservoir, representing potential undercooling of 50–110 °C. Only small to moderate degrees of undercooling (≤ 25 °C) are required to generate skeletal growth textures (Shea et al. 2019), so the magma that fed the 2020 eruption was most likely sourced from the south caldera reservoir and a deeper origin for the olivine crystals is not required.

Recycled crystals

X-ray maps of P zoning in two olivine crystals from this diffusion dataset (Fig. 5) and a third from this eruption in Mourey et al. (2023; their Fig. 2) display remarkable sharp, curved truncation surfaces delineating older regions of P-rich lamellae and younger regions of P-poor olivine overgrowths. Because the truncations occur at the ends of primary branches (red lines in Fig. 5), or where crystal faces meet, Mourey et al. (2023) interpreted these to be
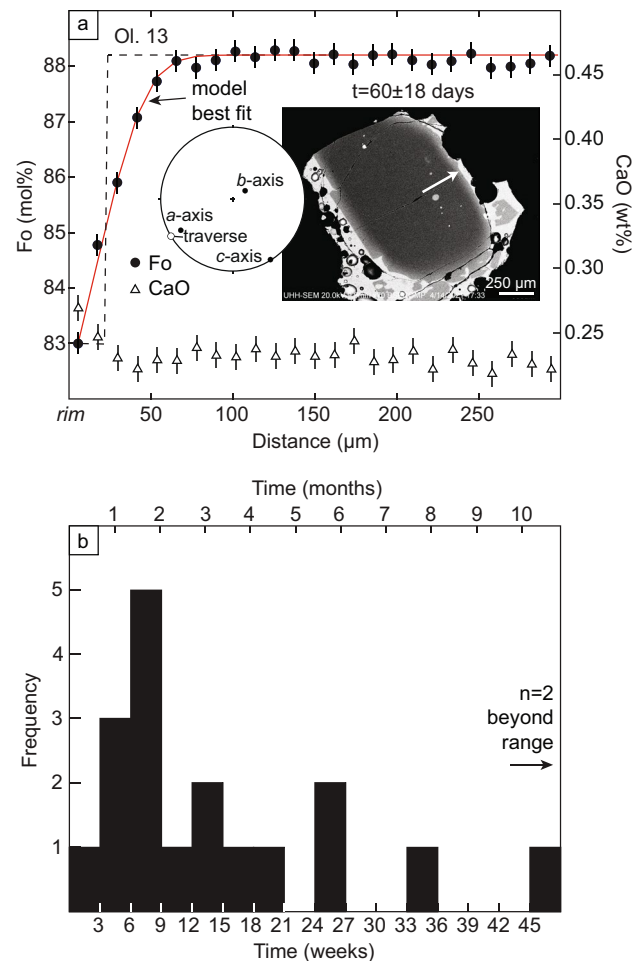
Fig. 6 a Example of electron backscatter diffraction data (shown as a lower hemisphere projection; Cardozo and Allmendinger 2013) and diffusion model results for normally zoned olivine #13 (Table 1), shown in the backscattered electron image. Model input conditions (dashed lines) and model best fit (red line) are shown for the Fo profile (black circles with uncertainty). Change in CaO (triangles) near the rim shows rationale for initial condition step function. **b** Twenty calculated timescales of diffusive re-equilibration from 19 olivine crystals (shoulder timescales plotted separately). Most crystals record timescales on the order of 4 months or less and half of the crystals record timescales of 3 months or less

unequivocally dissolution features, not crystal growth textures. We invoke the same interpretation here. The 2020 eruption olivine crystals experienced at least two dissolution–recrystallization cycles, followed by the final rim overgrowth (Fig. 5) as evidenced by (1) the innermost crystal core defined by primary and secondary branches in P zoning, followed by dissolution illustrated by the curved truncations of that zoning, and (2) growth of uniformly low-P, high-Fo over the first resorbed core, followed by dissolution again generating a rounded morphology on which, (3) the final overgrowth rim grew (on average) ~60–90 days prior to the 2020 eruption.

We note that the dissolution fronts within the olivine crystals are in regions of uniformly high-forsterite contents, indicating that the olivine crystals' early history included recycling within primitive melts (generating Fo_{88} or higher), which may have occurred within a mushy zone at the base of the south caldera reservoir (Wieser et al. 2019, 2020; Mourey et al. 2023; Anderson et al. 2024). These textures and chemical zonation reflect an older history possibly unrelated to the eruptive events of 2020. However, Mourey et al. (2023) noted that dissolution–recrystallization cycles of high-Fo olivine crystals can occur in less than a year and so these textures could be related to the post-2018 recovery of the summit reservoir system, indicated by high rates of summit inflation following the 2018 events (Poland et al. 2019; Patrick et al. 2020).

Regardless of the origins of the early cycles of dissolution–recrystallization, the final recrystallization event of the overgrowth rim can be linked to the months of pre-eruptive unrest leading to the 2020 eruption. The correlated Ca zoning and P enrichment band indicate a final stage of rim overgrowth, and the Fe–Mg interdiffusion timescales following that crystal growth show that it was recent, within ~ 60–90 days prior to eruption. The final dissolution event (time n + 3 in Fig. 5) could have occurred when magma migrated to the shallower Halema'uma'u reservoir in October 2020, as high-Fo olivine can dissolve rapidly (a few hundreds of microns per hour) in Kīlauea's typical evolved summit reservoir liquids (in equilibrium with Fo_{80-82}; Mourey et al. 2023). Then, the overgrowth rim, driven by undercooling (see above section), grew and diffusively re-equilibrated with the high-Fo core until the eruption in December.

Correlation of olivine timescales with signals of pre-eruptive unrest

The majority of the zoned December 2020 olivine crystals constrain timescales of magma movement through Kīlauea's post-collapse plumbing system such that the timing correlates remarkably well with the timing of pre-eruptive seismicity. The longest timescales retrieved by this study are difficult to interpret because they form a tail in the distribution and do not cluster together (Fig. 6). These data might be an artifact of off-center or highly oblique sectioning (Shea et al. 2015a). However, the crystals with the longest timescales have high-Fo cores similar to the rest of the olivine population, indicating that they have not significantly lost their high-Fo cores due to prolonged diffusion and/or they do not have lower Fo cores as a result of off-center sectioning. The BSE images and zoning patterns, crystal faces, and EBSD orientations also indicate that four of the five crystals with the longest timescales (Ol. 5, 10, 15, 20, and 23) are

oriented down the *a*- or *b*-axis with the *c*-axis in the plane of the section. Only one (Ol. 20) shows evidence for the *c*-axis highly oblique to the plane of the section (see Supplementary Data). Thus, the greater length of these timescales may not be due to sectioning artifacts.

The crystals with the longest timescales may instead reliably represent months to years of storage, which is consistent with geodetic data and also has been observed at other volcanic systems around the world (e.g., Mayon, Philippines, Ruth and Costa 2021; Llaima, Chile, Ruth et al. 2018; Mount Etna, Italy, Kahl et al. 2015). At Kīlauea, olivine crystals with skeletal textures have previously been modeled to survive for several months under magmatic conditions (Shea et al. 2015b). If true, the longest 2020 timescales coincide with volcanic unrest at Kīlauea that was characterized by episodic earthquake swarms in January, April, and June of 2020 (Fig. 7) and ground inflation, both of which were likely from magma recharge, which in turn could have prompted cycles of dissolution followed by crystal rim growth. A gravity survey conducted in April 2019 coupled with deformation data suggested that magma had largely filled in collapse void space by that time and had begun repressurizing the summit (Poland et al. 2019), so these longer olivine timescales may record earlier migration of magma from south caldera reservoir depths into the shallow Halema'uma'u reservoir. We focus on the shorter timescales, however, considering the consistency of the main olivine populations and zoning patterns in this study, and a paucity of data to clearly support the longer timescales.

The olivine timescales are primarily on the order of 4 months or less, which corresponds to a similar period of increased earthquake frequency under Kīlauea's summit beginning in September 2020 (Fig. 7). Deformation recorded by the UWE tiltmeter at Kīlauea's summit also changed character in September, from frequent deflation-inflation events (DI; Anderson et al. 2015) superimposed on steady inflation to relatively steady tilt without DI events until late October 2020. The cause of deflation-inflation events remains unknown, and changes in event frequency are not uncommon. Nonetheless, DI events may reflect perturbations in pressure conditions in the Halema'uma'u reservoir and could be a consequence of transient interruption of magma supply from the south caldera reservoir to the Halema'uma'u reservoir (Anderson et al. 2015; Poland et al. 2021). Despite the uncertainty in the causes for these signals, it is interesting that the olivine diffusion dataset for the 2020 eruption correlates with changes in DI events. Olivine chemical zoning might thus provide an additional line of inquiry for investigating the causes of DI events in Kīlauea tilt data.

There were also changes in deformation at Kīlauea's summit starting in late September 2020. Pressurization of the south caldera reservoir, evidenced by increasing line length (Fig. 7a) between permanent GPS stations OUTL and AHUP just south
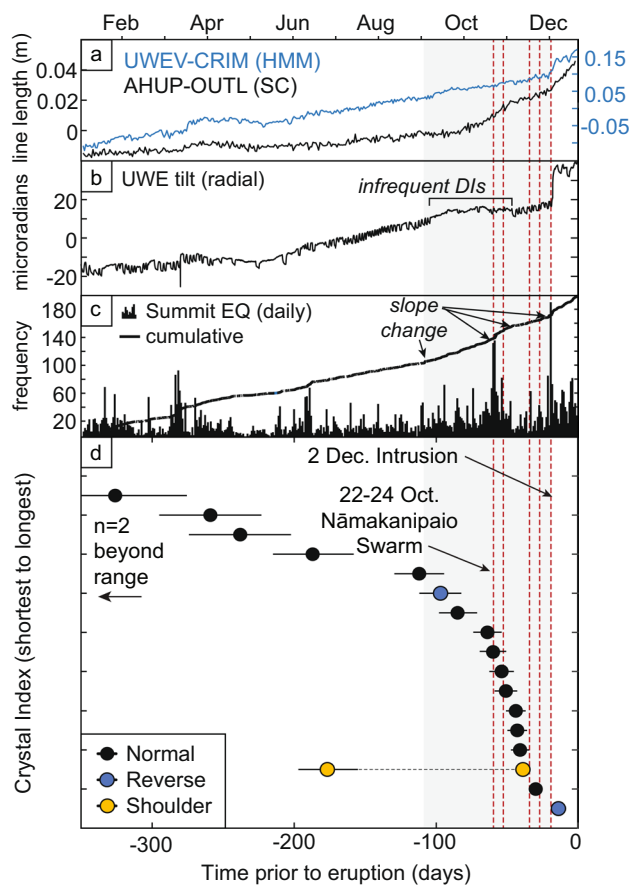
Fig. 7 Timeline of the 2020 pre-eruptive unrest, comparing **a** change in line length between UWEV and CRIM GPS stations (which are sensitive to changes in the Halemaʻumaʻu (HMM) reservoir; Segall and Miklius 1999a; Miklius 2008a) and AHUP and OUTL GPS stations (sensitive to the south caldera (SC) reservoir; Segall and Miklius 1999b; Miklius 2008b), **b** tilt at the UWE station (azimuth 327°; Ellis and Johanson 2024), **c** daily summit earthquakes (EQ, black bins) and cumulative earthquake counts (blue line; data available from the ANSS Comprehensive Earthquake Catalog, US Geological Survey, 2017), and **d** calculated olivine diffusion timescales (with ± 30% relative error). The two timescales retrieved for the complexly zoned "shoulder" profile (yellow circles) are connected by a dashed line. Station locations are shown in Fig. 1. Major earthquake swarm events and the 2 December intrusion are highlighted by the red dashed bars, and the September–November intrusion period is marked by light gray shaded field. There is a component of Kīlauea south flank motion in the GPS time series, but it was steady over the time period of interest and so the changes in the datasets are robust

of the summit caldera (Fig. 1a), increased from late September through October while the line length between GPS stations UWEV and CRIM across Halemaʻumaʻu (Fig. 1a) continued its inflation trend. Although the UWEV-CRIM inflation does not increase at the same magnitude as the AHUP-OUTL inflation, it does indicate a continued supply of magma to the shallower reservoir. The pressurization of the south caldera reservoir may have driven the upward movement of more crystal cargo at this time, as recorded by the olivine crystals.

The rate of summit seismicity was lower during the month of November 2020 and frequent DI events resumed with overall inflationary UWE tilt (Fig. 7) and slower rates but still increasing line length at UWEV-CRIM and AHUP-OUTL GPS sites. There was also a change in slope (and thus, a change in the frequency) in the calculated olivine timescales corresponding to the month of November. Fewer olivine diffusion timescales correlated with the lower levels of seismicity and return of DI events, hinting that rates of magma migration (recorded by the olivine crystals) might be tied to the presence or absence of DI events, which are still not well understood. If this is true, the previously sustained influx of magma might have become more episodic throughout November.

Only one olivine diffusion timescale aligns well with the 2 December 2020 summit intrusion, which occurred southeast of the post-2018 Halemaʻumaʻu collapse crater. This intrusion was distinct from the subsequent intrusion that fed the 20 December eruption vents, which opened on the west and northwest sides of the crater (Fig. 1). The lack of olivine diffusion timescales that correlate with the 2 December intrusion indicates that the event was not associated with an influx of magma from south caldera depths, and instead probably was an intrusion sourced from the Halemaʻumaʻu reservoir. Thus, at least two magma ascent pathways in the shallowest portions of Kīlauea's plumbing system above the Halemaʻumaʻu reservoir were created by intruding magma in the late months of 2020.

Tectonic versus magmatic signals

Half of the calculated timescales are 60 days or less and correlate well with the onset of 22–24 October earthquake swarms ~ 5 km west-northwest of Kīlauea's summit near the Nāmakani Paio Campground (Fig. 1). This is intriguing because the olivine record of magma storage and transport aligns with pre-eruptive unrest that is not associated with the physical location of the magmatic plumbing system (Fig. 8). The late October seismic swarm events were located between the Kaʻōiki fault system (a broad region between the summits of Kīlauea and Mauna Loa) and Kaluapele, Kīlauea's summit caldera, and are herein referred to as Nāmakani earthquakes (following the definition of Okubo and Nakata 2003). The structure associated with these earthquakes is a southeast-dipping normal fault at approximately 60° extending to 8 km depth toward Kaluapele (Okubo and Nakata 2003; Fig. 8).

Previous instances of Nāmakani earthquake swarms were related to episodes of the summit and upper East Rift Zone magma migration events between December 1990 and February 1993 during the Puʻuʻōʻō eruption (Okubo and Nakata 2003). Five different intrusion events during this time involved principally the upward transport of magma to shallower depths beneath the summit, and all were
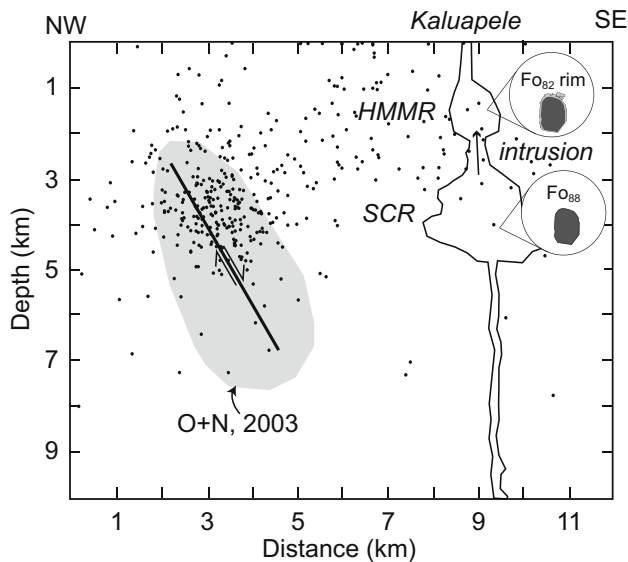
Fig. 8 Schematic cross section of Kīlauea along a southeast trend from the Nāmikani Paio region (Fig. 1) through the summit magmatic plumbing system. Black dots show hypocentral depths during the 22–24 October 2020 HST Nāmikani Paio swarm. Gray field denotes locations of hypocenters typical of Nāmakani Paio seismicity (interpolated from Okubo and Nakata 2003) caused by normal faulting in the Ka'ōiki fault system west of Kīlauea's summit. Olivine timescales that correlate with Nāmakani Paio earthquake swarms in late October 2020 indicate that crystals intruded from the south caldera reservoir (SCR) to the Halema'uma'u reservoir (HMMR) where Fo_{82} overgrowth rims formed and the diffusion clock started. Schematic of reservoir system geometry adapted from Anderson et al. (2024). Kaluapele is the new formal name for Kīlauea Caldera (USGS Geographic Names Information System)

associated with a recognizable cluster of tectonic Nāmakani earthquakes. This led to the interpretation that Nāmakani swarms were closely linked to changing regional stresses near Kīlauea's summit caldera (Okubo and Nakata 2003). Nāmakani seismicity was also elevated in 2005–2006 during a significant increase in magma supply to Kīlauea (Poland et al. 2012), further indicating that this fault system reacts to strong pressurization of the south caldera reservoir. We therefore interpret that the olivine timescales in the 2020 tephra record magma accumulation beneath Kīlauea's summit (volume accommodation) that was expressed by movement on nearby fault structures west-northwest of the summit caldera (stress accommodation). This distinction—correlating olivine diffusion timescales with non-magmatic (i.e., tectonic) seismic unrest—is important for diffusion studies and underscores the complexity of linking crystal archives with other types of volcano monitoring data.

Final brief ascent to the surface?

The 20 December 2020 eruption was immediately preceded by the most intense earthquake swarm detected in the months-long pre-eruptive sequence. The swarm began beneath Kaluapele around 20:30 HST, approximately 1 h prior to fissures breaking through the walls of Halema'uma'u. At the time, ground deformation was not significant and there were no changes in other monitoring data streams (Fig. 7). Almost all the relocated earthquakes from 20:30 HST until the eruption started had a median depth of 1.5 km (0.1 km standard deviation within the population and 0.3 km mean on the depth errors) and formed a linear east–west trending tangent under the south rim of Halema'uma'u. About 10 min prior to the start of the eruption, spasmodic tremor was also recorded underneath Kīlauea's summit. Spasmodic tremor (or classically VT [volcano-tectonic] earthquakes) is typically one of the earliest detectable precursors to volcanic activity (Roman and Cashman 2006) and generally represents magma migration (e.g., White and McCausland 2016). This suggests that the ascent of the 2020 magma from its storage region was brief—possibly traveling 1.5 km to the surface in as little as a few minutes. If the 2020 eruption magma ascended from 1.5 km (inferred depth from the crystal rim overgrowths) to the surface in 10 min or less, a linear ascent rate of 2.5 m/s can be calculated as a first-order approximation. This is a reasonable estimate for Hawaiian-style eruptions and is similar to a magma ascent rate calculated for phase 1 of the 1959 Kīlauea Iki eruption (~2 m/s) based on the decompression of an olivine-hosted melt embayment (Ferguson et al. 2016).

Data from the USGS Hawaiian Volcano Observatory's permanent gas monitoring network also suggest brief magma ascent prior to eruption. This includes data from several stations (Fig. 1) at the summit of Kīlauea for measuring SO_2, a volatile species that does not significantly degas until magma rises to ~200–150 m beneath the surface (< 2 MPa; Gerlach 1986). Prior to the onset of the 20 December eruption, during which there were prevailing northeasterly trade winds, no SO_2 was detected by the multi-GAS MG21_KIL and the high-resolution HRSDH ("Sand Hill") stations located south-southwest of the summit caldera (Fig. 9). The multi-GAS, which collects SO_2 data in cycles for ~35 min (with a temporal resolution of 2 s) every 3 h, fortuitously finished a data collection cycle just prior to the onset of the eruption at 21:30 HST. Despite this timing, no SO_2 was detected within minutes of the fissures breaking through the walls of Halema'uma'u. By the start of the next cycle at 00:00 HST on 21 December 2020, the multi-GAS recorded much higher ambient SO_2 from the degassing lava filling Halema'uma'u (Fig. 9). The Sand Hill station, which measures the average SO_2 concentration over 2 min once every 10 min, also recorded no ambient SO_2 prior to eruption and started registering detectible SO_2 values almost immediately after it started (Fig. 9). Thus, the gas data corroborate the interpretation that magma ascent probably occurred within a few minutes prior to eruption.
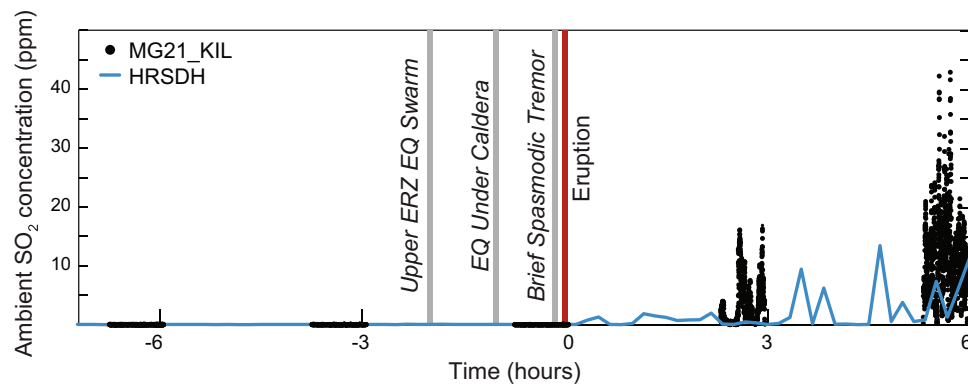
Fig. 9 Ambient SO_2 concentrations (ppm) in the several hours pre- and post-eruption on 20 December 2020 measured by two HVO monitoring stations south-southwest of the summit caldera (Fig. 1a). The multi-GAS (MG21_KIL) measures SO_2 in cycles for ~35 min (with a temporal resolution of 2 s) every 3 h (black dots). The Sand Hill high-resolution station (HRSDH) measures SO_2 for 2 out of every 10 min and records the average value (blue line). Based on sensor precision and average sensor response to standard gases, the total analytical error estimate for multi-GAS SO_2 is ± 15%. The high-resolution sensor is not tested against standard gases as often as the multi-GAS but the estimated total analytical error is less than that of the multi-GAS. These sensor performances were deemed acceptable for the present study; accordingly, we did not adjust the initial measured data values in post-processing. The East Rift Zone is abbreviated ERZ and earthquakes is abbreviated EQ in Fig. 9

When discussing a lack of precursory SO_2 emissions, particularly given the presence of a summit water lake at the time (Nadeau et al. 2020; Nadeau et al. 2024), we must consider the possibility that SO_2 was degassed from very shallow magma but ultimately scrubbed (e.g., Symonds et al. 2001) by groundwater or lake water prior to escape to the atmosphere. A water sample was collected from the lake on 26 October 2020, nearly coincident with the Nāmakani Paio earthquake swarms and olivine timescales that indicate magma was moving upward through the system. Because no samples were collected after that time, we cannot fully exclude the possibility of chemical changes in the lake related to scrubbing after the seismic swarms. Chemical changes, however, would likely be accompanied by changes in lake color or temperature, yet USGS Hawaiian Volcano Observatory staff did not find any evidence of significant changes in the water lake color, temperature, or rate of rise in the weeks and months prior to the 2020–2021 eruption (Patrick et al. 2021, 2023) and there were no changes observed by summit webcams in the minutes to hours preceding the breach of the fissures (Cahalan et al. 2023). It therefore seems likely that, rather than the water lake scrubbing substantial amounts of SO_2, the absence of precursory SO_2 was due solely to magma storage deep enough to suppress significant sulfur exsolution until the onset of magma ascent from 1-2 km shortly prior to eruption.

Conclusions

The 2020–2021 Halemaʻumaʻu eruption at Kīlauea volcano began on 20 December and produced a tephra deposit that contains a bimodal olivine population. Normally zoned high-Fo (Fo_{88}) olivine crystals, observed for the first time since the establishment of the 2008–2018 Halemaʻumaʻu lava lake, are interpreted to reflect an intrusion of deeper (likely from 3–5 km) magma to shallow levels (1–2 km) beneath Kīlauea's summit. Non-zoned Fo_{82} crystals and Fo_{82} skeletal crystal rims on zoned crystals are in Fe–Mg equilibrium with the host melt. There is no significant evidence of magma mixing between the intrusion that carried the normally zoned population and any resident magma leftover after the 2018 summit collapse, even though the Halemaʻumaʻu reservoir likely only drained 11–33% of its volume during the 2018 eruption (Anderson et al. 2019). Diffusion timescales calculated from zoned crystals show that magma from at least the depth of the south caldera reservoir (3–5 km) migrated to a depth of 1–2 km from September to November 2020. The intrusion caused undercooling, which prompted skeletal growth of both the Fo_{82} rims and a non-zoned olivine population of the same composition. Diffusion modeling of the zoned population yields timescales that correlate with regional tectonic seismicity near the Kaʻōiki fault zone, an area previously associated with regional stress changes related to high rates of magma storage at the summit. The diffusion data also correspond to a period of increased seismicity under Kīlauea's summit and heightened rates of inflationary summit deformation, indicating a sustained influx of magma to shallow levels. Only one olivine timescale aligns with the 2 December summit intrusion, underscoring the observation that mineral chronometers may not record all facets of the run-up to volcanic eruptions. Spasmodic tremor ~10 min prior to eruption and the lack of precursory SO_2 emissions indicates a high likelihood of very brief, possibly rapid final ascent of

the magma feeding the eruption. Combined, these data link together physical records of pre-eruptive magma migration recorded by the olivine crystals with the monitoring signals used as a proxy for how that migration is expressed as pre-eruptive unrest.

References

Albert H, Larrea P, Costa F, Widom E, Siebe C (2020) Crystals reveal magma convection and melt transport in dyke – fed eruptions. Sci Rep 10:11632. https://doi.org/10.1038/s41598-020-68421-4

Anderson KR, Shea T, Lynn KJ, Montgomery-Brown E, Swanson D, Patrick M, Shiro B, Neal T (2024) The 2018 eruption of Kīlauea: insights, puzzles, and opportunities for volcano science. An Rev Earth Planet Sci 52:11–139. https://doi.org/10.1146/annurev-earth-031621-075925

Anderson KR, Johanson IA, Patrick MP, Gu M, Segall P, Poland MP, Montgomery-Brown EK, Miklius A (2019) Magma reservoir failure and the onset of caldera collapse at Kīlauea Volcano in 2018. Science 366:eaaz1822. https://doi.org/10.1126/science.aaz1822

Anderson KR, Poland M, Johnson JH, Miklius A (2015) Episodic deflation-inflation events at Kīlauea Volcano and implications for the shallow magma system. In: Carey C, Poland W (eds) Hawaiian Volcanoes: From Source to Surface. American Geophysical Union Monograph, p 229–250. https://doi.org/10.1002/9781118872079.ch11

Armstrong JT (1988) Quantitative analyses of silicate and oxide mate- rials: comparison of Monte Carlo, ZAF, and φ(ρz) procedures Microbeam analyses. San Francisco Press, San Francisco, pp 239–246

Burgess MK, Roman DC (2021) Ongoing (2015-) magma surge in the upper mantle beneath the island of Hawai'i. Geophys Res Lett 48(7):1–10. https://doi.org/10.1029/2020GL091096

Cahalan RC, Mastin LG, Van Eaton AR, Hurwitz S, Smith AB, Dufek J, Solovitz SA, Patrick M, Schmith J, Parcheta C, Thelen WA, Downs DT (2023) Dynamics of the December 2020 ash-poor plume formed by lava-water interaction at the summit of Kīlauea Volcano, Hawai'i. Geochem Geophys Geosyst 24:e2022GC010718. https://doi.org/10.1029/2022GC010718

Cardozo N, Allmendinger RW (2013) Spherical Projections with OSXStereonet. Comp Geosci 51:193–205. https://doi.org/10.1016/j.cageo.2012.07.021

Cervelli PF, Miklius A (2003) The shallow magmatic system of Kilauea Volcano. USGS Prof Pap 1676:149–163

Chakraborty S (2010) Diffusion coefficients in olivine, wadsleyite and ringwoodite. Rev Mineral Geochem 72:603–639. https://doi.org/10.2138/rmg.2010.72.13

Coogan LA, Hain A, Stahl S, Chakraborty S (2005) Experimental determination of the diffusion coefficient for calcium in olivine between 900°C and 1500°C. Geochim Cosmochim Acta 69:3682–3694. https://doi.org/10.1016/j.gca.2005.03.002

Corbi F, Rivalta E, Pinel V, Maccaferri F, Bagnardi M, Acocella V (2015) How caldera collapse shapes the shallow emplacement and transfer of magma in active volcanoes. Earth Planet Sci Lett 431:287–293. https://doi.org/10.1016/j.epsl.2015.09.028

Costa F, Shea T, Ubide T (2020) Diffusion chronometry and the timescales of magmatic processes. Nat Rev Earth Env 1:201–204. https://doi.org/10.1038/s43017-020-0038-x

Costa F, Dungan M (2005) Short time scales of magmatic assimilation from diffusion modeling of multiple elements in olivine. Geology 33:837–840. https://doi.org/10.1130/G21675.1

Costa F, Chakraborty S (2004) Decadal time gaps between mafic intrusion and silicic eruption obtained from chemical zoning patterns in olivine. Earth Planet Sci Lett 224:517–530. https://doi.org/10.1016/j.epsl.2004.08.011

Crank J (1975) The mathematics of diffusion, 2nd edn. Oxford Science Publications, Oxford

de Maisonneuve CB, Costa F, Huber C, Vonlanthen P, Bachmann O, Dungan MA (2016) How do olivines record magmatic events? Insights from major and trace element zoning. Cont Mineral Petrol 171(6):1–20. https://doi.org/10.1007/s00410-016-1264-6

Dohmen R, Faak K, Blundy JD (2017) Chronometry and speedometry of magmatic processes using chemical diffusion in olivine, plagioclase, and pyroxenes. Rev Mineral Geochem 83:535–575. https://doi.org/10.2138/rmg.2017.83.16

Dohmen R, Chakraborty S (2007a) Fe-Mg diffusion in olivine II: point defect chemistry, change of diffusion mechanisms and a model for calculation of diffusion coefficients in natural olivine. Phys Chem Miner 34(6):409–430. https://doi.org/10.1007/s00269-007-0158-6

Dohmen R, Chakraborty S (2007b) Erratum on "Fe–Mg diffusion in olivine II: point defect chemistry, change of diffusion mechanisms and a model for calculation of diffusion coefficients in natural olivine." Phys Chem Miner 34:597–598. https://doi.org/10.1007/s00269-007-0185-3

Ellis AP, Johanson IA (2024) Tiltmeter data from Kīlauea summit station UWE from January 1 to December 31, 2020. U. S. Geological Survey data release. https://doi.org/10.5066/P13SWUMJ

Ellis AP, Johanson IA, Chang J, Flinders A, Kamibayashi K, McLay M, Phillips DA, Poland M (2023) Geodetic network upgrades and recent deformation signals at Kīlauea volcano. IAVCEI 2023 Scientific Assembly, Rotorua, New Zealand, p 584

Faure F, Schiano P (2004) Crystal morphologies in pillow basalts: implications for mid-ocean ridge processes. Earth Planet Sci Lett 145:331–344. https://doi.org/10.1016/S0012-821X(04)00057-3

Faure F, Schiano P, Trolliard G, Nicollet C, Soulestin B (2007) Textural evolution of polyhedral olivine experiencing rapid cooling

rates. Cont Mineral Petrol 153:405–416. https://doi.org/10.1007/s00410-006-0154-8

Ferguson DJ, Gonnermann HM, Ruprecht P, Plank T, Hauri EH, Houghton BF, Swanson DA (2016) Magma decompression rates during explosive eruptions of Kīlauea volcano, ©, recorded by melt embayments. Bull Volcanol 78:71. https://doi.org/10.1007/s00445-016-1064-x

Flinders AF, Kauahikaua JP, Hsieh PA, Ingebritsen SE (2021) Post audit of simulated groundwater flow to a short-lived (2019 to 2020) crater lake at Kīlauea Volcano. Groundwater 60:64–70. https://doi.org/10.1111/gwat.13133

Gansecki C, Lee RL, Shea T, Lundblad SP, Hon K, Parcheta C (2019) The tangled tale of Kīlauea's 2018 eruption as told by geochemical monitoring. Science 366:eaaz0147. https://doi.org/10.1126/science.aaz0147

Garcia MO, Pietruszka AJ, Rhodes JM (2003) A petrologic perspective of Kīlauea's summit magma reservoir. J Petrol 44:2313–2339. https://doi.org/10.1093/petrology/egg079

Gavrilenko M, Ozerov A, Kyle PR, Carr MJ, Nikulin A, Vidito C, Danyushevsky L (2016) Abrupt transition from fractional crystallization to magma mixing at Gorely volcano (Kamchatka) after caldera collapse. Bull Volcanol 78:1–47. https://doi.org/10.1007/s00445-016-1038-z

Gerlach TM (1986) Exsolution of H_2O, CO_2, and S during eruptive episodes at Kilauea Volcano, Hawai'i. J Geophys Res 91(B12):12177–12185. https://doi.org/10.1029/JB091iB12p12177

Gordeychik B, Churikova T, Shea T, Kronz A, Simakin A, Wörner G (2020) Fo and Ni relations in olivine differentiate between crystallization and diffusion trends. J Petrol 61:egaa083. https://doi.org/10.1093/petrology/egaa083

Gordeychik B, Churikova T, Kronz A, Sundermeyer C, Simakin A, Wörner G (2018) Growth of, and diffusion in, olivine in ultrafast ascending basalt magmas from Shiveluch volcano. Sci Rep 8:11775. https://doi.org/10.1038/s41598-018-30133-1

Hartley ME, Morgan DJ, Maclennan J, Edmonds M, Thordarson T (2016) Tracking timescales of short-term precursors to large basaltic fissure eruptions through Fe-Mg diffusion in olivine. Earth Planet Sci Lett 439:58–70. https://doi.org/10.1016/j.epsl.2016.01.018

Helz RT (2022) Proportions, timing, and re-equilibration progress during the 1959 summit eruption of Kīlauea: an example of magma mixing processes operating during OIB petrogenesis. J Petrol 63(1):1–22. https://doi.org/10.1093/petrology/egab091

Helz RT, Thornber CR (1987) Geothermometry of Kilauea Iki lava ©Hawaii. Bull Volcanol 49(5):651–668. https://doi.org/10.1007/BF01080357

Helz RT, Cottrell E, Brounce MN, Kelley KA (2017) Olivine-melt relationships and syneruptive redox variations in the 1959 eruption of Kīlauea Volcano as revealed by XANES. J Volcanol Geotherm Res 333–334:1–14. https://doi.org/10.1016/j.jvolgeores.2016.12.006

Holzapfel C, Chakraborty S, Rubie DC, Frost DJ (2007) Effect of pressure on Fe-Mg, Ni, and Mn diffusion in $(Fe_xMg_{1-x})_2SiO_4$ olivine. Phys Earth Planet Inter 162:186–198. https://doi.org/10.1016/j.pepi.2007.04.009

Jambon A, Lussiez P, Clocchiatti R, Weisz J, Hernandez J (1992) Olivine growth rates in tholeiitic basalt: an experimental study of melt inclusions in plagioclase. Chem Geol 96:277–287. https://doi.org/10.1016/0009-2541(92)90059-E

Jarosewich E, Nelen JA, Norberg JA (1980) Reference samples for electron microprobe analysis. Geos News 4(1):43–47. https://doi.org/10.1111/j.1751-908X.1980.tb00273.x

Kahl M, Chakraborty S, Pompilio M, Costa F (2015) Constraints on the nature and evolution of the magma plumbing system of Mt.

Etna Volcano (1991–2008) from a combined thermodynamic and kinetic modeling of the compositional records of minerals. J Petrol 56:2025–2068. https://doi.org/10.1093/petrology/egv063

Kahl M, Chakraborty S, Costa F, Pompilio M (2011) Dynamic plumbing system beneath volcanoes revealed by kinetic modeling, and the connection to monitoring data: an example from Mt. Etna Earth Planet Sci Lett 308:11–22. https://doi.org/10.1016/j.epsl.2011.05.008

Kilgour GN, Saunders KE, Blundy JD, Cashman KV, Scott BJ, Miller CA (2014) Timescales of magmatic processes at Ruapehu volcano from diffusion chronometry and their comparison to monitoring data. J Volcanol Geotherm Res 288:62–75. https://doi.org/10.1016/j.volgeores.2014.09.010

Lang S, Mollo S, France L, Misiti V, Nazzari M (2021) Kinetic partitioning of major-minor cations between olivine and Hawaiian tholeiitic basalt under variable undercooling and cooling rate conditions. Chem Geol 584:120485. https://doi.org/10.1016/j.chemgeo.2021.120485

Lerner AH, Wallace PJ, Shea T, Mourey AJ, Kelly PJ, Nadeau PA, Elias T, Kern C, Clor LE, Gansecki C, Lee RL, Moore LR, Werner CA (2021) The petrologic and degassing behavior of sulfur and other magmatic volatiles from the 2018 eruption of Kīlauea, Hawai'i: melt concentrations, magma storage depths, and magma recycling. Bull Volcanol 83:43. https://doi.org/10.1007/s00445-021-01459-y

Lynn KJ (2022) Olivine and glass analyses for select eruptions of Kilauea Volcano, Hawai'i. U.S. Geological Survey Data Release. https://doi.org/10.5066/P9HA3PRK

Lynn KJ, Helz RT (2023) Magma storage and transport timescales for the 1959 Kīlauea Iki eruption and implications for diffusion chronometry studies using time-series samples versus tephra deposits. Bulletin of Volcanology 85(1). https://doi.org/10.1007/s00445-022-01618-9

Lynn KJ, Swanson DA (2022) Olivine and glass chemistry record cycles of plumbing system recovery after summit collapse events at Kīlauea Volcano, Hawai'i. J Volcanol Geotherm Res 426:107540. https://doi.org/10.1016/j.jvolgeores.2022.107540

Lynn KJ, Garcia MO, Shea T, Costa F, Swanson DA (2017a) Timescales of mixing and storage for Keanakāko'i Tephra magmas (1500–1820 C.E.), Kīlauea Volcano, Hawai'i. Cont Mineral Petrol. 172(9). https://doi.org/10.1007/s00410-017-1395-4

Lynn KJ, Shea T, Garcia MO (2017b) Nickel variability in Hawaiian olivine: evaluating the relative contributions from mantle and crustal processes. Am Mineral 102:507–518. https://doi.org/10.2138/am-2017-5763

Matzen AK, Baker MB, Beckett JR, Stolper EM (2011) Fe–Mg partitioning between olivine and high-magnesian melts and the nature of Hawaiian parental liquids. J Petrol 52:1243–1263. https://doi.org/10.1093/petrology/egq089

Miklius A (2008a) Hawaii GPS Network - CRIM-Crater Rim P.S., GAGE Facility, GPS/GNSS Observations Dataset. 10.7283/T5RR1WGN

Miklius A (2008b) Hawaii GPS Network - OUTL-Outlet P.S., GAGE Facility, GPS/GNSS Observations Dataset. 10.7283/T5WH2N7T

Millman-Barris MS, Beckett JR, Michael MB, Hofmann AE, Morgan Z, Crowley MR, Vilzeuf D, Stolper E (2008) Zoning of phosphorus in igneous olivine. Contrib Mineral Petrol 155:739–765. https://doi.org/10.1016/j.epsl.2011.05.008

Montierth C, Johnston AD, Cashman KV (1995) An empirical glass-composition-based geothermometer for Mauna Loa lavas. In: Rhodes, Lockwood (eds) Mauna Loa Revealed: Structure, Composition, History, and Hazards. American Geophysical Union Monograph, 92, 207–217

Mosbrucker AR, Zoeller MH, and Ramsey DW (2020) Digital elevation model of Kīlauea Volcano, Hawai'i, based on July 2019 airborne

lidar surveys: U.S. Geological Survey data release. https://doi.org/10.5066/P9F1ZU8O

Mourey AJ, Shea T, Hammer JE (2023) Preservation of magma recharge signatures in Kīlauea olivine during protracted storage. J Geophys Res Solid Earth 128:e2022JB025523. https://doi.org/10.1029/2022JB025523

Mourey AJ, Shea T, Lynn KJ, Lerner AH, Lambart S, Costa F, Oalmann J, Lee RL, Gansecki C (2022) Trace elements in olivine fingerprint the source of 2018 magmas and shed light on explosive-effusive eruption cycles at Kīlauea Volcano. Earth Planet Sci Lett 595:117769. https://doi.org/10.1016/j.epsl.2022.117769

Nadeau PA, Hurwitz S, Peek S, Lerner AH, Younger EF, Patrick MR, Damby DE, McCleskey RB, Kelly PJ (2024) Physical and chemical evolution of the short-lived (2019–2020), historically unprecedented crater lake at the summit of Kīlauea Volcano, Hawaii. Geochem Geophys Geosyst 25:e2023GC011154. https://doi.org/10.1029/2023GC011154

Nadeau PA, Diefenbach AK, Hurwitz S, Swanson DA (2020) From lava to water: a new era at Kīlauea. EOS, 101, published on 25 September 2020. https://doi.org/10.1029/2020EO149557

Neal CA et al (2019) The 2018 rift eruption and summit collapse of Kīlauea Volcano. Science 363(6425):367–374. https://doi.org/10.1126/science.aav7046

Office for Coastal Management (2015) 2005 Hawaii IfSAR Digital Terrain Model (DTM). https://www.fisheries.noaa.gov/inport/item/48377. Accessed 2015

Okubo P, Nakata JS (2003) Tectonic pulses during Kīlauea's current long-term eruption. U.S. Geological Survey Prof Pap 1676:173–186

Patrick MR, Parcheta C, Nadeau P, Downs D, Zoeller M, Lynn KJ (2023) Colorimeter data for the summit water lake at Kīlauea Volcano, Hawaii, 2020: U.S. Geological Survey data release. https://doi.org/10.5066/P95WBNRV

Patrick MR, Swanson DA, Zoeller MH, Mulliken KM, Parcheta CE, Lynn KJ, Downs DT, Flinders AF (2021) Water-level data for the crater lake at the summit of Kīlauea Volcano, Island of Hawai'i, 2019–2020: U.S. Geological Survey data release. https://doi.org/10.5066/P9262JDH

Patrick MR, Houghton BF, Anderson KR, Poland MP, Montgomery-Brown E, Johanson I, Thelen W, Elias T (2020) The cascading origin of the 2018 Kīlauea eruption and implications for future forecasting. Nat Comm 11:5646. https://doi.org/10.1038/s41467-020-19190-1

Petry C, Chakraborty S, Palme H (2004) Experimental determination of Ni diffusion coefficients in olivine and their dependence on temperature, composition, oxygen fugacity, and crystallographic orientation. Geochim Cosmochim Acta 68:4179–4188. https://doi.org/10.1016/j.gca.2004.02.024

Pietruszka AJ, Heaton DE, Marske JP, Garcia MO (2015) Two magma bodies beneath the summit of Kīlauea Volcano unveiled by isotopically distinct melt deliveries from the mantle. Earth Planet Sci Lett 413:90–100. https://doi.org/10.1016/j.epsl.2014.12.040

Pietruszka AJ, Garcia MO (1999) The size and shape of Kilauea Volcano's summit magma storage reservoir: a geochemical probe. Earth Planet Sci Lett 167:311–320. https://doi.org/10.1016/S0012-821X(99)00036-9

Poland MP, Miklius A, Johanson IA, Anderson KR (2021) A decade of geodetic change at Kīlauea's summit—observations, interpretations, and unanswered questions from studies of the 2008–2018 Halema'uma'u eruption, chap. G of Patrick M, Orr T, Swanson D, and Houghton B (eds). The 2008–2018 summit lava lake at Kīlauea Volcano, Hawai'i: U.S. Geological Survey Professional Paper 1867, 29. https://doi.org/10.3133/pp1867G

Poland MP, de Zeeuw-van Dalfsen E, Bagnardi M, Johanson IA (2019) Post-collapse gravity increase at the summit of Kīlauea Volcano, Hawai'i. Geophys Res Lett 46. https://doi.org/10.1029/2019GL084901

Poland MP, Miklius A, Montgomery-Brown E (2014) Magma supply, storage, and transport at shield-stage Hawaiian volcanoes. In: Poland MP, Takahashi TJ, Landowski CM (eds) Characteristics of Hawaiian volcanoes. US Geological Survey, Washington, DC, pp 179–234. https://doi.org/10.3133/pp18015

Poland MP, Miklius A, Sutton AJ, Thornber CR (2012) A mantle-driven surge in magma supply to Kīlauea Volcano during 2003–2007. Nat Geosci 5(4):295–300. https://doi.org/10.1038/ngeo1426

Rasmussen D, Plank T, Roman D, Power JA, Bodnar RJ, Hauri EH (2018) When does eruption run-up begin? Multidisciplinary insight from the 1999 eruption of Shishaldin volcano. Earth Planet Sci Lett 486:1–14. https://doi.org/10.1016/j.epsl/2018.01.001

Roeder PL, Emslie RF (1970) Olivine-liquid equilibrium. Cont. Mineral Petrol 29:275–289. https://doi.org/10.1007/BF00371276

Roman DC, Cashman KV (2006) The origin of volcano-tectonic earthquake swarms. Geology 34:457–460. https://doi.org/10.1130/G22269.1

Ruth DCS, Costa F (2021) A petrological and conceptual model of Mayon volcano (Philippines) as an example of an open-vent volcano. Bull Volcanol 83(10). https://doi.org/10.1007/s00445-021-01486-9

Ruth DCS, Costa F, de Maisonneuve CB, Cortés JA, Calder ES, Franco L (2018) Crystal and melt inclusion timescales reveal the evolution of magma migration before eruption. Nat Commun 9:2657. https://doi.org/10.1038/s41467-018-05086-8

Saunders K, Blundy J, Dohmen R, Cashman K (2012) Linking petrology and seismology at an active volcano. Science 336:1023–1027. https://doi.org/10.1126/science.1220066

Schleicher J (2017) Crystal-scale control on magmatic mush mobilization and mixing. Doctoral dissertation, p 103. https://digital.lib.washington.edu/researchworks/handle/1773/40392

Segall P, Anderson K, Wang TA. 2022. Could Kīlauea's 2020 post caldera-forming eruption have been anticipated? Geophys Res Lett 49(15):e2022GL099270

Segall P, Miklius A (1999a) Hawaii GPS Network - UWEV-Uwekahuna Vault P.S., GAGE Facility, GPS/GNSS Observations Dataset. https://doi.org/10.7283/T51C1TXB

Segall P, Miklius A (1999b) Hawaii GPS Network - AHUP-Ahua P.S., GAGE Facility, GPS/GNSS Observations Dataset. https://doi.org/10.7283/T5ST7MW0

Shea T, Matzen AK, Mourey AJ (2022) Experimental study of Fe-Mg partitioning and zoning during rapid growth of olivine in Hawaiian tholeiites. Cont Mineral Petrol 177:114. https://doi.org/10.1007/s00410-022-01969-8

Shea T, Hammer JE, Hellebrand E, Mourey AJ, Costa F, First EC, Lynn KJ, Melnik O (2019) Phosphorous and aluminum zoning in olivine: contrasting behavior of two nominally incompatible trace elements. Cont Mineral Petrol 174:85. https://doi.org/10.1007/s00410-019-1618-y

Shea T, Costa F, Krimer D, Hammer JE (2015a) Accuracy of timescales retrieved from diffusion modeling in olivine: a 3D perspective. Am Mineral 100:2026–2042. https://doi.org/10.2138/am-2015-5163

Shea T, Lynn KJ, Garcia MO (2015b) Cracking the olivine zoning code: distinguishing between crystal growth and diffusion. Geology 43:935–938. https://doi.org/10.1130/G37082

Symonds RB, Gerlach TM, Reed MH (2001) Magmatic gas scrubbing: implications for volcano monitoring. J Volcanol Geotherm Res 108:303–341. https://doi.org/10.1016/S0377-0273(00)00292-4

Thornber CR, Orr TR, Heliker C, Hoblitt RP (2015) Petrologic testament to changes in shallow magma storage and transport during

30+ years of recharge and eruption at Kīlauea Volcano, Hawai'i. Am Geophys Mono 208:147–188

Tilling RI, Dvorak JJ (1993) Anatomy of a basaltic volcano. Nature 363:125–133

U.S. Geological Survey (1983) 20230522, USGS 1/3 Arc Second n20w156 20230522: U.S. Geological Survey. www.sciencebase.gov/catalog/item/646c4889d34ee02593fb4b4d. Accessed 2023

U.S. Geological Survey (2017) Advanced National Seismic System (ANSS) Comprehensive Catalog of Earthquake Events and Products. Earthquake Hazards Program. https://doi.org/10.5066/F7MS3QZH. Accessed 2023

Wang T, Zheng Y, Pulvirenti F, Segall P (2021) Post-2018 caldera collapse re-inflation uniquely constrains Kīlauea's magmatic system. J Geophys Res Solid Earth 126(6):e2021JB021803

Wang Z, Gaetani GA (2008) Partitioning of Ni between olivine and siliceous eclogite partial melt: experimental constraints on the mantle source of Hawaiian basalts. Contrib Mineral Petrol 156:661–678. https://doi.org/10.2138/am-2017-5763

Welsch B, Hammer J, Hellebrand E (2014) Phosphorus zoning reveals dendritic architecture Of olivine. Geology 42(10):867–870. https://doi.org/10.1130/G35691.1

Welsch B, Faure F, Famin V, Baronnet A, Bachèlery P (2013) Dendritic crystallization: a single process for all the textures of olivine In basalts? J Petrol 54(3):539–574. https://doi.org/10.1093/petrology/egs077

White R, McCausland W (2016) Volcano-tectonic earthquakes: a new tool for estimating intrusive volumes and forecasting eruptions. J Volcanol Geotherm Res 309:139–155 (j.jvolgeores.2015.10.020)

Wieser PE, Lamadrid H, Maclennan J, Edmonds M, Matthews S, Iacovino K, Jenner FE, Gansecki C, Trusdell F, Lee RL, Ilyinskaya E (2021) Reconstructing magma storage depths for the 2018 Kīlauean eruption from melt inclusion CO_2 contents the importance of vapor bubbles. Geochem Geophys Geosyst. 22:e2020GC009364

Wieser PE, Edmonds M, Maclennan J, Wheeler J (2020) Microstructural constraints on magmatic mushes under Kīlauea Volcano, Hawai'i. Nat Comm 11:14. https://doi.org/10.1038/s41467-019-13635-y

Wieser PE, Edmonds M, Maclennan J, Jenner FE, Kunz BE (2019) Crystal scavenging from mush piles recorded by melt inclusions. Nat Comm 10:5797. https://doi.org/10.1038/s41467-019-13518-2

Wilding JD, Zhu W, Ross ZE, Jackson JM (2022) The magmatic web beneath Hawai'i. 5755:1–14

Wright TL, Peck DL (1978) Crystallization and differentiation©e Alae magma, Alae lava lake Hawaii USGS. Prof Pap 935:1–19. https://doi.org/10.3133/pp935C

Wright TL, Okamura RT (1977) Cooling and crystallization of tho©c basalt, 1965 Makaopuhi Lava Lake Hawaii USGS. Prof Pap 1004:1–78. https://doi.org/10.3133/pp1004